Journal of Materials Chemistry C

ROYAL SOCIETY OF CHEMISTRY

PAPER

View Article Online
View Journal | View Issue



Cite this: J. Mater. Chem. C, 2026, 14, 7868

# Excitation-selective coexistence of upconversion and persistent luminescence in $Pr^{3+}$-doped eulytite-type phosphates towards advanced anti-counterfeiting

Guna Doke, *[ab] Andris Antuzevics,[b] Didzis Salnajs,[b] Nadiia Rebrova,[c] Alexander Grippa,[d] Przemysław J. Dereń,[c] Aldona Beganskiene[a] and Aleksej Zarkov[a]

This work demonstrates the excitation-selective coexistence of blue-light-driven UVC upconversion (UC), X-ray-induced optical luminescence (XRL), and persistent luminescence (PersL) within a single $Pr^{3+}$-doped host lattice. $Pr^{3+}$-doped $Ba_3Lu(PO_4)_3$ and $Sr_3Lu(PO_4)_3$ phosphors exhibit multiple excitation-dependent luminescence modes and are studied as multifunctional materials for advanced anti-counterfeiting. When excited with blue light (444 nm), they efficiently produce blue-to-UVC upconversion *via* an excited-state absorption mechanism, while direct ultraviolet and visible excitation trigger characteristic $Pr^{3+}$ photoluminescence. X-ray irradiation induces intense blue–red optical luminescence, followed by long-lasting red persistent luminescence detectable for several hours at room temperature. Thermally stimulated luminescence (TSL) and electron paramagnetic resonance (EPR) measurements were employed to elucidate the nature of charge trapping processes that produce persistent emission. The TSL glow curves of all samples are dominated by a semi-broadband peak around 70 °C, indicative of a quasi-continuous distribution of trapping states. $T_{max}$–$T_{stop}$ experiments combined with initial rise analysis reveal trap depths between 0.9–1.15 eV, supporting effective room-temperature PersL. EPR spectroscopy identifies radiation-induced phosphorus-related radical centers and shallow traps, which most likely correspond to $F^+$-type centers, with thermal stability matching TSL results. These findings highlight the potential of $Pr^{3+}$-doped eulytite-type phosphates as versatile, multi-level luminescent platforms for advanced anti-counterfeiting and encryption solutions.

Received 30th January 2026,
Accepted 13th March 2026

DOI: 10.1039/d6tc00314a

rsc.li/materials-c



## 1. Introduction

Advanced anti-counterfeiting technologies increasingly depend on multi-modal luminescent materials capable of generating complex, adjustable optical responses under various excitation sources.[1–3] Traditional photoluminescent systems, while effective for basic fluorescent tagging, often lack multi-excitation responsiveness and long-lasting emission needed for secure authentication. To address these limits, recent research has focused on designing multimodal phosphors that exhibit upconversion (UC), persistent luminescence (PersL), and other optical processes triggered by specific excitation, such as ultraviolet (UV), visible (VIS), or ionizing radiation.[4–9]

UC luminescence involves absorbing lower-energy photons and then emitting higher-energy photons, enabling high-contrast emission and enhancing security through unique excitation pathways.[10–12] In contrast, high-energy irradiation-induced PersL provides long-lasting emission even after the excitation source is switched off.[13,14] Combining these different excitation methods in a single material offers a powerful strategy for multilevel security encoding, creating optical signatures that are nearly impossible to replicate. Although there is extensive research on anti-counterfeiting applications for UC or PersL materials, there is a notable lack of studies that address both processes within the same material.

$Pr^{3+}$-activated phosphors are attractive luminescent materials due to their rich energy-level structure, which enables emissions spanning from the UV to VIS spectral regions under different excitation pathways. Materials doped with $Pr^{3+}$ exhibit efficient 4f5d-4f emission, as well as intra-4f transitions, and

[a] Institute of Chemistry, Vilnius University, Naugarduko 24, LT-03225 Vilnius, Lithuania. E-mail: guna.doke@cfi.lu.lv
[b] Institute of Solid State Physics, University of Latvia, Kengaraga 8, LV-1063 Riga, Latvia
[c] Institute of Low Temperature and Structure Research, Polish Academy of Science, ul. Okólna 2, 50-422 Wrocław, Poland
[d] Institute for Scintillation Materials, National Academy of Sciences of Ukraine, Nauky Avenue, 60, 61001, Kharkiv, Ukraine

excitation-dependent processes such as UC or defect-mediated recombination.[7,15–18] Eulytite-type orthophosphates with the formula $A_3M(PO_4)_3$ (A = Ca, Sr, Ba, Pb; M = La–Lu, Y, Sc, Bi, In) are widely investigated as hosts for rare-earth phosphors because of their large band gaps, high chemical and thermal stability, water resistance, low sintering temperatures, and excellent optical properties. Among these materials, $Ba_3Lu(PO_4)_3$ and $Sr_3Lu(PO_4)_3$ are particularly promising, as they accommodate various activators and energy transfer pathways.[19–23] Recently, Rebrova *et al.*[24] have discovered unusually effective blue-to-UVC upconversion luminescence in $Pr^{3+}$-doped $Ba_3Lu(PO_4)_3$ and $Sr_3Lu(PO_4)_3$ phosphors, with potential uses in sterilization, disinfection, photocatalysis, and phototherapy. Simultaneously, there is no information on X-ray-induced optical luminescence (XRL), PersL, or thermally stimulated luminescence (TSL) in these materials.

In this study, we demonstrate that $Ba_3Lu(PO_4)_3$ and $Sr_3Lu(PO_4)_3$ exhibit multimodal luminescence, which includes blue light-excited UVC UC and X-ray-induced blue-red XRL, along with red PersL and TSL, and traditional photoluminescence (PL) under direct excitation. The synergistic interaction among these emissions creates a versatile optical system with excitation-dependent color changes and temporally distinct luminescent modes. Such materials open new possibilities for advanced anti-counterfeiting applications, where dynamic, multi-stimulus luminescent responses provide strong protection against forgery and enable quick, contactless authentication.

## 2. Experimental

### 2.1. Preparation of phosphors

Powder samples of $A_3Lu_{1-x}Pr_x(PO_4)_3$ (A = Sr, Ba; $x$ = 0–0.02) were prepared using the Pechini sol–gel method.[25] Analytical-grade reagents $Lu_2O_3$, $SrCO_3$, $BaCO_3$, $NH_4H_2PO_4$, $Pr_2O_3$, citric acid, and ethylene glycol were used without further purification. Stoichiometric amounts of $Lu_2O_3$, $ACO_3$, and $Pr_2O_3$ were dissolved in nitric acid under mild heating to produce a clear solution, which was then recrystallized to remove excess acid. Next, aqueous solutions of citric acid, $NH_4H_2PO_4$, and ethylene glycol were added (molar ratio 2 : 2 : 1 for citric acid:ethylene glycol:metal cations) under continuous stirring. The mixture was heated at 80 °C for 24 hours to form a viscous white resin, which was then calcined in two steps: 500 °C for 6 hours to eliminate organics, followed by 1250 °C for 5 hours to produce the crystalline phosphate phase.

### 2.2. Measurements and characterization

The crystal structure of the samples was characterized by X-ray powder diffraction (XRD) using an X'Pert PRO X-ray diffractometer with a Cu Kα radiation source over a $2\theta$ range of 5°–80°.

The PL and PL excitation (PLE) spectra were recorded using an Edinburgh Instruments FLS 1000 spectrofluorometer equipped with a CW 450 W Xe lamp and a cooled Hamamatsu R928P photomultiplier tube (PMT). UC spectra measurements were performed using a VUV McPherson spectrometer equipped with a Hamamatsu R7154P PMT, a UG5 filter (Eksma Optics), and 444 nm continuous-wave laser excitation.

TSL glow curves, XRL, and PersL measurements were measured using a Lexsyg research Fully Automated TL/OSL Reader from Freiberg Instruments GmbH. The irradiation sources were an X-ray tube (40 kV, 0.5 mA, W-anode). The measurements were recorded with a Hamamatsu R13456 PMT or an Andor Technology SR-303i-B spectrometer coupled with a DV420A-BU2 CCD camera. When measuring TSL, the system operated at a linear heating rate of 1 °C $s^{-1}$. The same system was used to measure isothermal PersL decay curves. A Nikon D3300 digital camera was used to capture images of the XRL and PersL at shutter speeds of 1 and 10 s, respectively, at ISO 3600 and f/5.6.

Room-temperature EPR spectra were measured using a Bruker ELEXSYS-II E500 CW-EPR spectrometer operating at 9.836 GHz and 10 mW microwave power. The magnetic field modulation amplitude was 0.4 mT, with a modulation frequency of 100 kHz. An X-ray tube operated at 45 kV and 10 mA for 10 min was used to investigate the radiation-induced radicals in the samples. Afterwards, the irradiated samples were isochronally annealed in an air atmosphere, maintaining each temperature step for 10 min, using a custom-built furnace.

To enable a direct comparison among phosphors, all samples were synthesized using the same protocol and measured under strictly identical experimental conditions. Powder samples were pressed into identical sample holders to ensure comparable geometry and optical density. Excitation sources, irradiation times, detection settings, and heating protocols were held constant across all measurements.

## 3. Results and discussion

### 3.1. Phase and structure analysis

Fig. 1 represents the XRD patterns of $Ba_3Lu(PO_4)_3$: $x$% $Pr^{3+}$ and $Sr_3Lu(PO_4)_3$: $x$% $Pr^{3+}$ powders with different $Pr^{3+}$ concentration (0 to 2 mol%). All diffraction peaks align well with the standard card and can be indexed to a cubic structure with space group $I\bar{4}3d$. Additionally, the phase purity of $Ba_3Lu(PO_4)_3$ and $Sr_3Lu(PO_4)_3$ materials was confirmed by using the Rietveld refinement result, which can be seen in Supporting Information Fig. S1 and S2.

The eulytite structure is intrinsically disordered, as demonstrated by Barbier[26] for $Ba_3La(PO_4)_3$. Substitution of La with Lu does not modify the structural framework. By analogy with previous reports, it can therefore be assumed that in the investigated samples $Ba^{2+}$ (or $Sr^{2+}$ in $Sr_3Lu(PO_4)_3$) randomly occupies the same C3 crystallographic site as $Lu^{3+}$ (or in a doped structure $Pr^{3+}$), with site occupation factors of approximately 0.75 for the divalent cation and 0.25 for the trivalent cation.[27] The presence of cations with different charges sharing the same lattice site leads to the formation of two possible orientations of the $[PO_4]^{3-}$ tetrahedra within the (Sr, Ba, Lu)$_8$ bisphenoid units. As a result, the (Ba, Sr)$_3$Lu(PO$_4$)$_3$ phase exhibits not only cation disorder but also oxygen sublattice disorder, reflected by two distinct oxygen positions with site

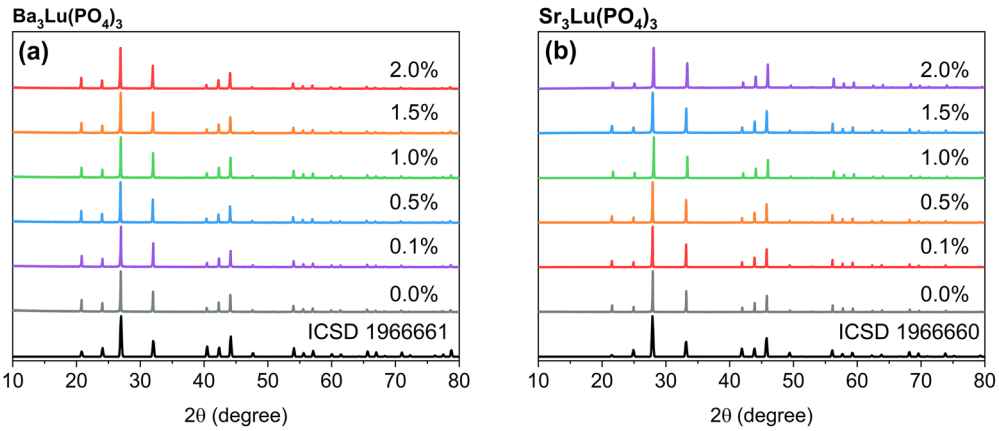


Fig. 1 XRD patterns of $Pr^{3+}$-doped (a) $Ba_3Lu(PO_4)_3$ and (b) $Sr_3Lu(PO_4)_3$ samples.

occupation factors of approximately 0.35 and 0.65. From a spectroscopic perspective, this structural disorder results in a distribution of local crystal-field environments experienced by $Pr^{3+}$ ions. Consequently, inhomogeneous broadening of emission lines is observed, along with multi-exponential decay kinetics indicative of site-selective relaxation pathways. Moreover, the coexistence of nonequivalent $Pr^{3+}$ sites and local defect configurations may facilitate carrier trapping, thereby contributing to PersL lasting for tens of minutes after excitation is removed.

### 3.2. PL, XRL, and UC luminescence properties

The PLE spectra of 1.0% $Pr^{3+}$ doped samples are shown in Fig. 2(a). A broad UV excitation band around 200–250 nm and multiple overlapping VIS excitation bands around 420–500 nm are observed. These bands are attributed to intra-center transitions of $Pr^{3+}$ ions from the ground state $^3H_4$ to the 4f5d or $^3P_J$ levels, respectively. The simplified energy level scheme with relevant transitions is depicted in Fig. 3.[28,29] The PL emission spectra of 1.0% $Pr^{3+}$-doped samples, recorded under excitation at 220 and 440 nm, are presented in Fig. 2(b). Under deep-UV excitation, the emission spectra exhibit multiple bands corresponding to radiative transitions from the 4f5d state to the $^3H_J$ and $^3F_J$ manifolds of $Pr^{3+}$ ions, resulting in a broad UVC luminescence band. In comparison, the luminescence in the VIS spectral range at this excitation is almost negligible. This indicates an extremely low non-radiative transition probability

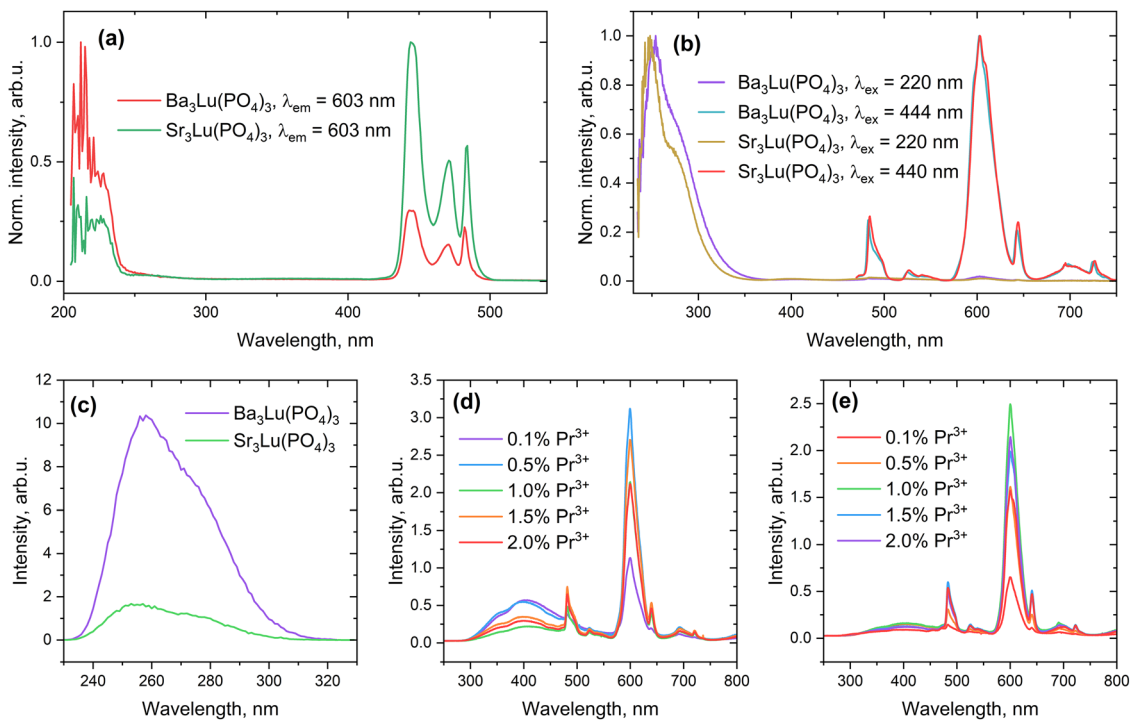


Fig. 2 (a) PLE spectra of 1.0% $Pr^{3+}$ samples ($\lambda_{em}$ = 603 nm); (b) PL spectra of 1.0% $Pr^{3+}$ samples ($\lambda_{ex}$ = 220 and 440 nm); (c) UC spectra of 1.5% samples, excited with 444 nm; (d) XRL of $Ba_3Lu(PO_4)_3$ samples (e) $Sr_3Lu(PO_4)_3$ samples.

 

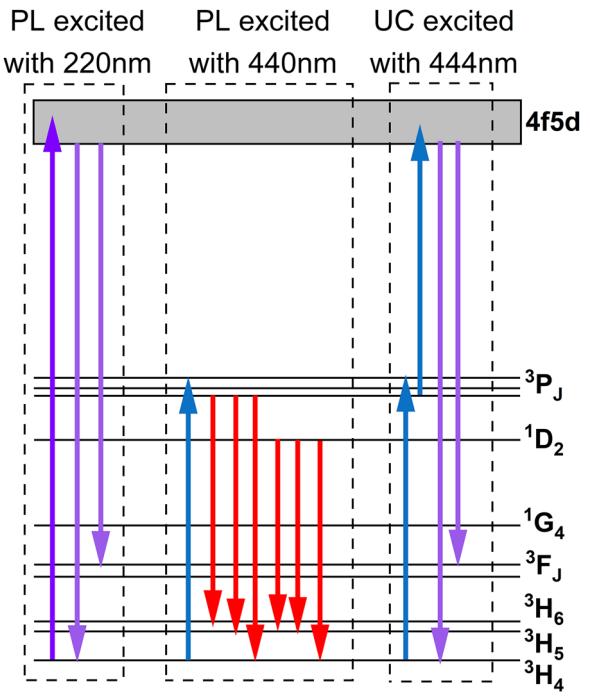


Fig. 3 The schematic energy level diagram of $Pr^{3+}$ and possible mechanisms of PL after irradiation with 220 and 440 nm, and possible UC mechanism after irradiation with 444 nm in $Ba_3Lu(PO_4)_3$: $Pr^{3+}$ and $Sr_3Lu(PO_4)_3$: $Pr^{3+}$ materials.

from 4f5d to lower-energy levels, such as the $^3P_J$ manifold. When materials are excited at 440 nm, multiple $Pr^{3+}$ typical VIS PL bands appear,[4,30,31] with a dominant line with a maximum at 603 nm, corresponding to the $^3P_0 \rightarrow {}^3H_4$ optical transition. On the other hand, experiments have shown that the 444 nm excitation wavelength can induce UC in these materials; namely, the sequential absorption of two or more 444 nm photons promotes $Pr^{3+}$ ions from the ground state $^3H_4$ through intermediate $^3P_J$ levels to higher lying 4f5d states. This is called the excited-state absorption (ESA) mechanism,[17,32] and its presence in these materials has been previously proved.[24] Subsequent radiative relaxation from these high-energy states results in UVC emission between 240 and 300 nm, with a maximum at *ca.* 255 nm. The ESA mechanism in $Pr^{3+}$ ions is demonstrated in Fig. 3, while UC spectra recorded with 444 nm excitation are shown in Fig. 2(c).

Overall, these findings show that $Pr^{3+}$ doped $Ba_3Lu(PO_4)_3$ and $Sr_3Lu(PO_4)_3$ phosphors exhibit excitation-dependent emission behavior. This tunable excitation capability enables the simultaneous presence of multiple luminescence modes within the same material when optically excited. In addition, while not explored here, Rebrova *et al.*[24] showed that lifetime values of the $^3P_0$ and $^1D_2$ levels of $Pr^{3+}$ in these materials vary by two orders of magnitude, with $\tau(^3P_0)$ *ca.* 2–3 μs and $\tau(^1D_2)$ *ca.* 300–400 μs; therefore, a visible PL signal can easily be used for fast dynamic anti-counterfeiting solutions based on time-gated detection.

$Pr^{3+}$-doped $Ba_3Lu(PO_4)_3$ and $Sr_3Lu(PO_4)_3$ phosphors can also be excited with X-rays. Fig. 2(d) and (e) show the corresponding XRL spectra, and the first row in Fig. 5 depicts digital photos of the samples under X-ray excitation. The same optical transitions observed in 440 nm-excited PL are present, with additional broadband luminescence between 300 and 600 nm. This type of broadband luminescence is typically associated with host-related defect recombination.[33,34] The host-related XRL bands are particularly prominent in low-concentration $Pr^{3+}$-doped $Ba_3Lu(PO_4)_3$, making it highly desirable for achieving color-tunable anti-counterfeiting. Notably, there is no UVC emission under X-ray excitation, indicating that the 4f5d level remains unpopulated. The $^3P_J$ and $^1D_2$ levels, responsible for visible emission, appear to be populated directly under high-energy excitation. Similar behaviour has been reported in earlier spectroscopic studies. In $Y_3Al_5O_{12}:Pr^{3+}$ crystals and films[35] Zorenko *et al.* observed that excitation above the host bandgap or within the excitonic absorption region results in emission spectra dominated by narrow 4f–4f lines in the visible range. A comparable effect was demonstrated for $BaF_2:Pr^{3+}$ by Drozdowski and Wojtowicz.[36] They showed that excitation within the excitonic band suppresses broadband 5d → 4f emission. Similar behaviour has also been reported for $LiNaY_2F_8:Pr^{3+}$.[37]

As discussed by Gusowski *et al.*,[38] emission from excitonic states is associated with a large Stokes shift, indicative of strong lattice relaxation. Within the configurational coordinate framework, the relaxed excitonic-state potential may intersect directly with the $^3P_J$ manifold, enabling energy transfer to the 4f configuration without populating the 4f5d states. This results in the preferential observation of sharp 4f–4f emission lines in the VIS range.

In the case when the excitation energy is reduced (*i.e.*, longer excitation wavelengths are used) to directly excite the $4f^15d^1$ absorption bands, broadband 5d → 4f emission becomes observable, provided that the lowest 5d levels lie below the $^1S_0$ state.

In addition, following excitation of the host lattice, traps present in the matrix become populated. In addition to self-trapped excitons (STE), the matrix also supports defect-trapped excitons (DTE). The subsequent thermal release of energy from these traps *via* DTE recombination can directly populate the $^3P_0$ level, providing a pathway contributing to the observed visible emission.

### 3.3. Persistent luminescence properties

Under X-rays, charge carriers are efficiently generated in the host lattice and subsequently trapped at intrinsic defect sites, as evident by the presence of broadband defect-related XRL. After cessation of X-ray irradiation, the gradual thermal release of these trapped carriers leads to their recombination at $Pr^{3+}$ luminescent centers, resulting in a PersL signal. The spectra of 1.0% $Pr^{3+}$ samples and PersL decay kinetics of all $Ba_3Lu(PO_4)_3$ and $Sr_3Lu(PO_4)_3$ samples are shown in Fig. 4. After switching off the X-rays, the host-related luminescence disappears, and only $Pr^{3+}$ VIS range luminescence bands can be observed. Consistent with the XRL mechanism described above, the recombination of thermally released carriers proceeds *via* localized defect- and

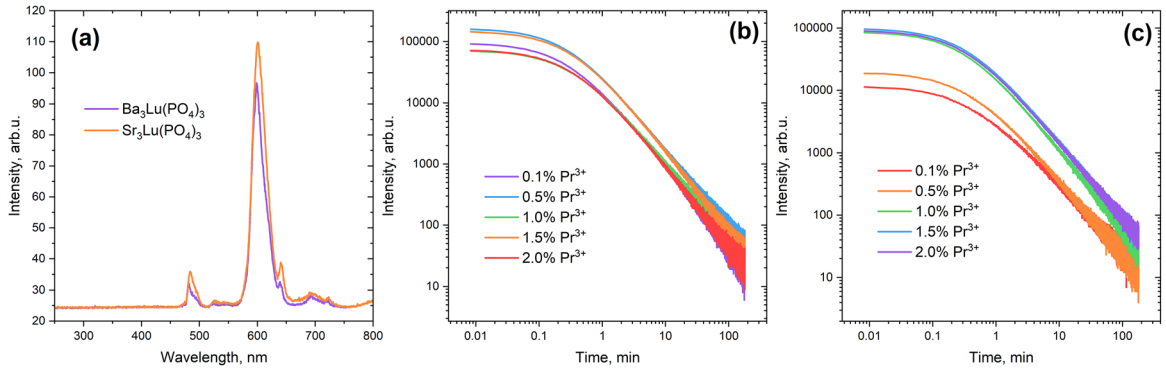


Fig. 4 (a) PersL spectra of 1.0% $Pr^{3+}$ samples and PersL decay kinetics of (b) $Ba_3Lu(PO_4)_3$ and (c) $Sr_3Lu(PO_4)_3$ samples after irradiation with X-rays.

exciton-related states that transfer energy directly to the $Pr^{3+}$ $^3P_J$ manifold without populating the 4f5d configuration. If recombination occurred *via* fully delocalized carrier transport, the spectral profile would resemble that of XRL. Instead, the selective population of $Pr^{3+}$ VIS-emitting levels indicates recombination mediated by localized defect states and defect-trapped excitons, whose relaxation transfers energy to the 4f configuration.

For both sets of samples, the PersL can be detected for at least 2 hours, and no changes other than the intensity of the spectra were observed during this time. Fig. 5 shows the digital images of PersL change for the first three minutes.

### 3.4. Trap analysis

For a detailed analysis of defect properties, TSL and EPR measurements were performed. Fig. 6 shows the TSL glow curves of the $Ba_3Lu(PO_4)_3:Pr^{3+}$ and $Sr_3Lu(PO_4)_3:Pr^{3+}$ samples after X-ray irradiation. The heating rate was 1 °C $s^{-1}$. The TSL glow curves of all investigated samples exhibit a single, semi-broadband glow peak with a maximum around 70 °C. However, despite the apparent single-peak character, the profile and width of the glow peak suggest that it is composed of multiple closely overlapping components rather than originating from a single discrete trapping level, indicating a quasi-continuous trap distribution, which typically means that the respective defects have disordered surroundings. The disordered local environment was already discussed above. Furthermore, the non-zero TSL intensity observed at room temperature indicates the presence of traps whose true glow-peak maxima are likely below room temperature. The highest TSL intensity is observed in samples with a $Pr^{3+}$ doping concentration of around 1.5%, which coincides with PersL observations.

To better understand the trap properties, $T_{max}$–$T_{stop}$ experiments combined with initial rise analysis (IRA) were conducted on one representative sample from each series. Both methods are widely acknowledged and used in the analysis of thermally unstable defects.[39–43] In the $T_{max}$–$T_{stop}$ method, the sample undergoes repeated irradiation and preheating to increasingly higher $T_{stop}$ temperatures, and the residual TSL glow curves are then recorded. Tracking how $T_{max}$, the peak maximum temperature, changes can reveal details about the trap distribution. Specifically, if $T_{max}$ rises steadily with $T_{stop}$, it indicates a continuous trap distribution. Conversely, if $T_{max}$ remains

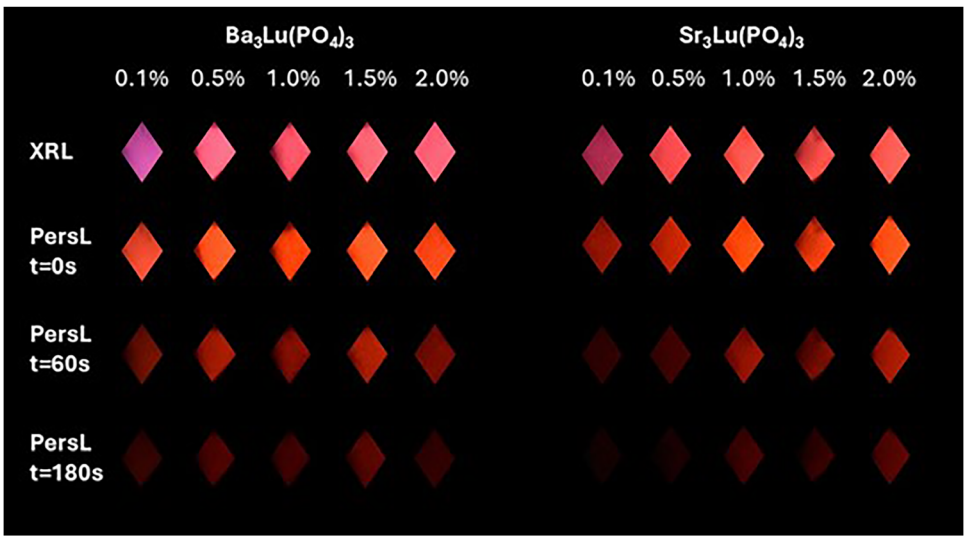


Fig. 5 Digital images of the XRL and PersL of $Pr^{3+}$-doped $Ba_3Lu(PO_4)_3$ and $Sr_3Lu(PO_4)_3$ samples at different periods after cessation of X-ray excitation.

 

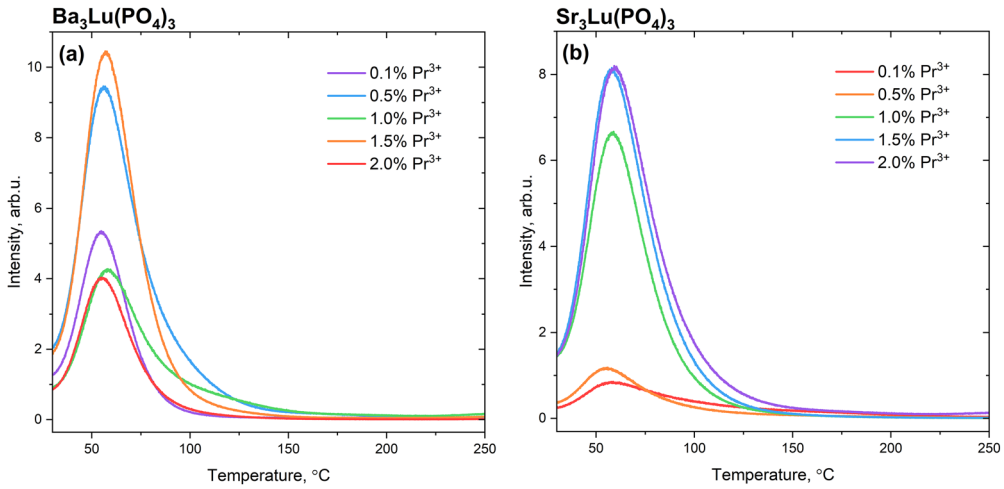


Fig. 6 TSL glow curves of $Pr^{3+}$-doped (a) $Ba_3Lu(PO_4)_3$ and (b) $Sr_3Lu(PO_4)_3$ samples after irradiation with X-rays.

unchanged as $T_{stop}$ increases, the trap can be identified as discrete. The results of the $T_{max}$–$T_{stop}$ experiment are shown in Fig. 7. Fig. 7(a) and (d) show TSL glow curves of the $Ba_3Lu(PO_4)_3$ : 1.5% $Pr^{3+}$ and $Sr_3Lu(PO_4)_3$ : 1.5% $Pr^{3+}$ samples after preheating to different $T_{stop}$ values between 30 and 125 °C in 5 °C steps. The $T_{max}$–$T_{stop}$ plots are shown in Fig. 7(c) and (f) as orange and red squares, respectively. From these plots, it is confirmed that the traps present in $Pr^{3+}$ doped $Ba_3Lu(PO_4)_3$ and $Sr_3Lu(PO_4)_3$, by their nature, are continuously distributed rather than a set of well-separated discrete trap levels. A quasi-continuous trap distribution explains the prolonged PersL decay seen at room temperature, since charge carriers are slowly released from traps with varying thermal stabilities. The glow curves obtained in the $T_{max}$–$T_{stop}$ experiment were used in IRA to determine the activation energy ($E_a$) or trap depth of the corresponding defects. IRA is based on the assumption that, in the low-temperature region of a TSL glow peak, the luminescence intensity is governed by thermally activated release of charge carriers from traps and follows an Arrhenius-type behavior:

$$I(T) = C \cdot \exp\left(-\frac{E_a}{k_B T}\right) \quad (1)$$

Here, $I(T)$ is the TSL intensity as a function of temperature, $C$ is a constant that includes the frequency factor and is assumed to be

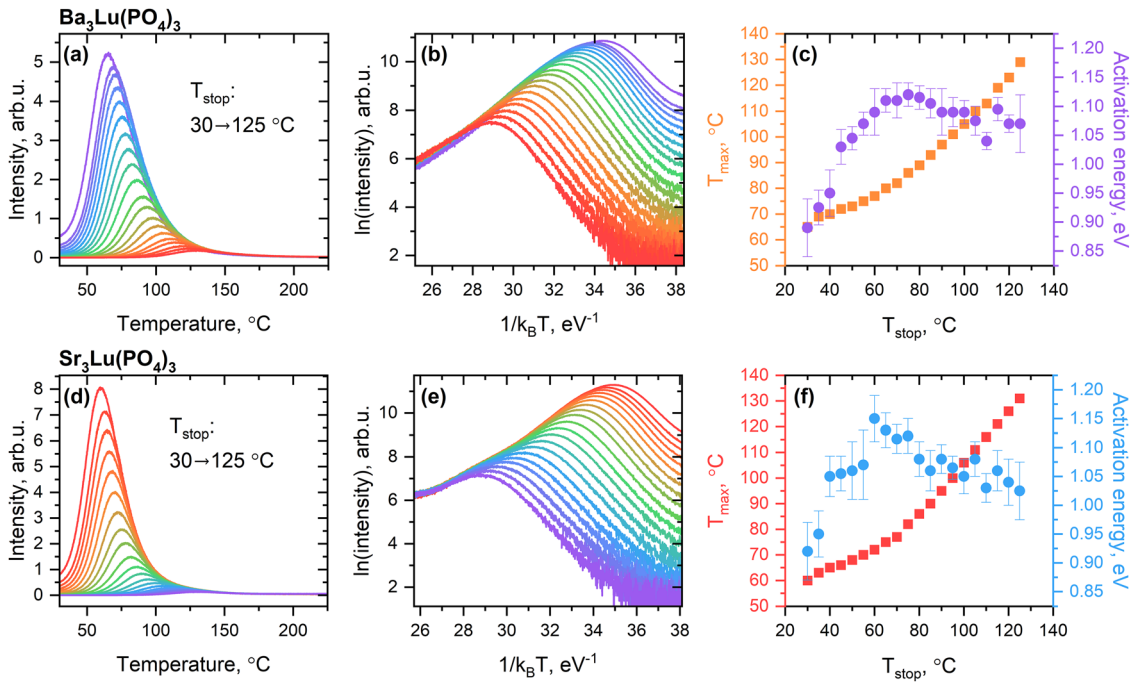


Fig. 7 TSL glow curves of the (a) $Ba_3Lu(PO_4)_3$ : 1.5% $Pr^{3+}$ and (d) $Sr_3Lu(PO_4)_3$ : 1.5% $Pr^{3+}$samples after preheating up to different $T_{stop}$ values between 30 and 125 °C with a 5 °C step. The samples were irradiated with X-rays for 20 s before each preheating; (b) and (e) IRA plots of the glow curves obtained from the $T_{max}$–$T_{stop}$ experiments; (c) and (f) corresponding$T_{max}$–$T_{stop}$/$E_a$–$T_{stop}$ plots.

temperature independent, $k_B$ is the Boltzmann constant, $T$ is the temperature, and $E_a$ represents the activation energy (trap depth). According to eqn (1), plotting $\ln(I)$ as a function of $(k_BT)^{-1}$ yields a linear dependence in the initial rise region of the glow peak. The slope of this linear fit corresponds to $-E_a$, allowing direct estimation of the trap depth without assumptions regarding the peak shape or kinetic order of the process. The IRA plots are shown in Fig. 7(b) and (e), and the corresponding plots of $T_{stop} - E_a$ are shown in Fig. 7(c) and (f) as purple and blue dots. The trap depths derived from the IRA analysis range from about 0.9 to 1.15 eV for both samples, which is near the values typically associated with effective room-temperature PersL, around 0.8 eV,[44,45] indicating efficient thermal release of charge carriers at ambient conditions. It is important to note that the early part of the trap distribution likely comprises shallower traps. However, because TSL measurements were only initiated at room temperature, these shallow traps are not reliably detectable in this study. Future low-temperature TSL experiments are necessary to fully characterize the shallow trap distribution. Altogether, the $T_{max}$–$T_{stop}$ and IRA results obtained for both $Ba_3Lu(PO_4)_3:Pr^{3+}$ and $Sr_3Lu(PO_4)_3:Pr^{3+}$ series are qualitatively and quantitatively similar, indicating comparable trapping mechanisms in both host lattices.

EPR spectroscopy was applied to gain additional insights into X-ray-induced charge trapping and luminescence processes in the investigated samples. A result summary is provided in Fig. 8, where the upper row displays EPR spectra of $Ba_3Lu(PO_4)_3:1.5\%$ $Pr^{3+}$, while the lower row shows those of $Sr_3Lu(PO_4)_3:1.0\%$ $Pr^{3+}$. The different EPR experiment sessions are grouped into columns: the left column compares spectra recorded before and after 10 min of X-ray irradiation; the middle column – temporal decay of EPR signals during storage at room temperature; the right column – evolution of the signals following stepwise sample annealing at selected temperatures.

A doublet at *ca.* 348 and 351 mT (labelled as "Signal 1") is generated by X-ray irradiation in both investigated hosts. This signal can be interpreted in two ways. One possibility is that it arises from two distinct paramagnetic centers with g-factors of 2.017 and 2.001, respectively. Alternatively, Signal 1 can be modelled as a single phosphorus-related paramagnetic center with an effective g-factor of 2.009 split into two components due to hyperfine (HF) interaction with a single $^{31}P$ nucleus with a HF splitting of about 3 mT. The relatively synchronous decay of the two components during both sample storage at room temperature (Fig. 8(b) and (e)) and stepwise annealing (Fig. 8(c) and (f)) supports the latter interpretation, indicating the formation of a PO-type radical. Radiation-induced $PO_4^{2-}$, $PO_3^{2-}$, and $PO_2^-$ radicals are well-documented in phosphate materials.[46–49] From these, $PO_4^{2-}$ seems the most plausible candidate for the interpretation of Signal 1 in $Ba_3Lu(PO_4)_3$ and $Sr_3Lu(PO_4)_3$ due to the relatively small HF splitting.

A relatively broad resonance at 356 mT ($g = 1.973$; "Signal 2") is additionally detected in the $Ba_3Lu(PO_4)_3$ sample. This signal corresponds to a shallow trap, as evidenced by its lower stability compared to Signal 1 (Fig. 8(e) and (f)). The g-factor shift from the free-electron $g_e = 2.0023$ value suggests that the wavefunction of the trapped electron is hybridized with the orbitals of

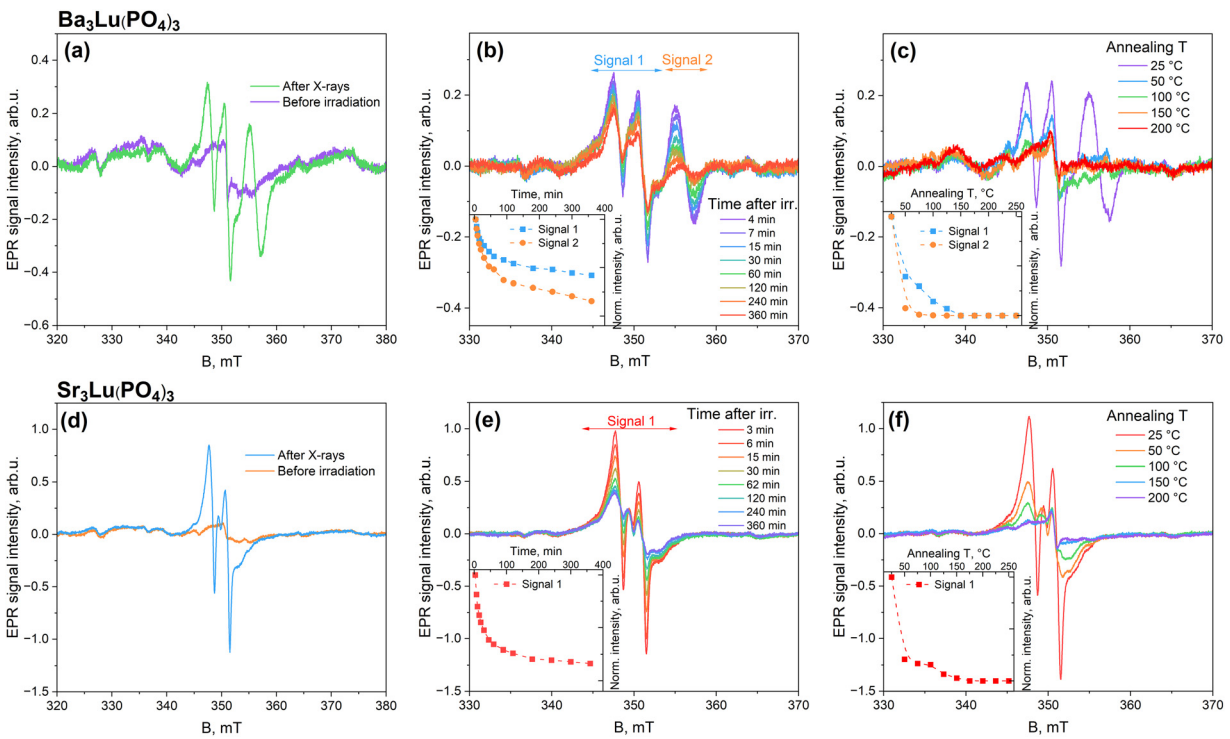


Fig. 8 EPR spectra of $Ba_3Lu(PO_4)_3:1.5\%$ $Pr^{3+}$ (top row) and $Sr_3Lu(PO_4)_3:1.0\%$ $Pr^{3+}$ (bottom row) samples: (a) and (d) before and after irradiation with X-rays; (b) and (e) following sample storage for different time intervals at room temperature; insets: decay of the radiation-induced EPR signals with time; (c) and (f) after sample annealing at selected temperatures; insets: annealing kinetics of the radiation-induced EPR signals.

 

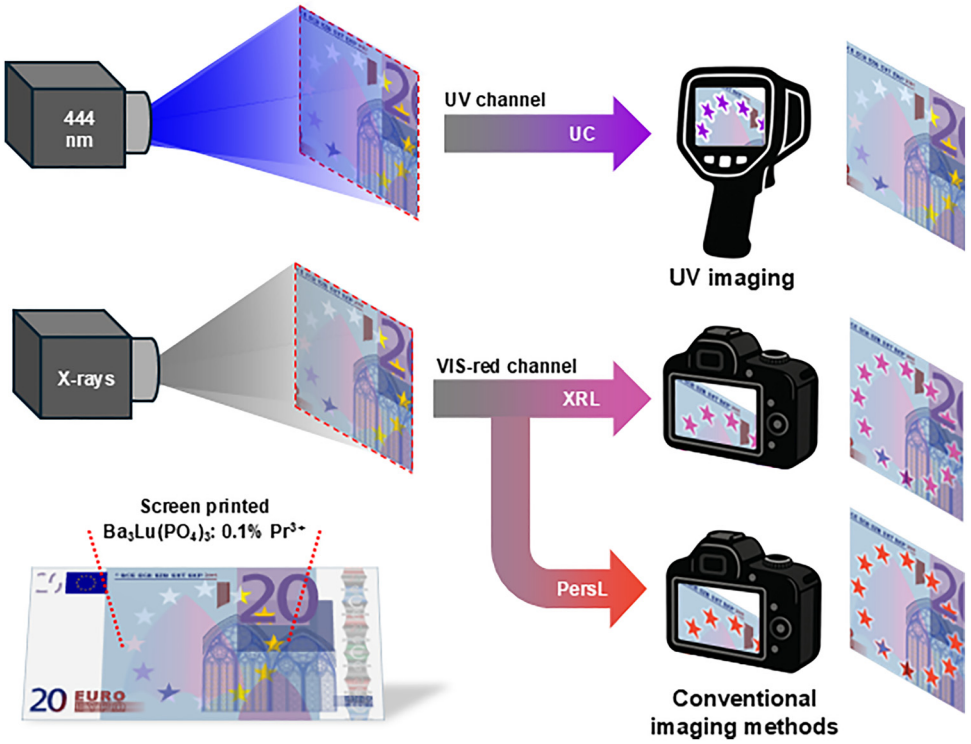


Fig. 9 Conceptual schematic illustration of dynamic multicolor anticounterfeiting and information encryption.

heavy cations ($Ba^{2+}$ or $Lu^{3+}$).[50] Large negative g-factor shifts have been reported for $F^+$-type centers – single trapped electrons at oxygen vacancies – in Ba-containing oxide materials.[51,52] In eulytite-type hosts, alternating cation occupancy and structural disorder in the oxygen sublattice may facilitate the formation of oxygen vacancy traps[27,53] and contribute to the substantial broadening of Signal 2. However, the g-factor value alone is insufficient for a definitive identification, and additional spectroscopic or theoretical evidence would be required to confirm its microscopic origin.

Stability experiments indicate that all detected paramagnetic centers contribute to X-ray-induced recombination luminescence processes. The annealing range of EPR signals (Fig. 8(c) and (f)) overlaps with the temperature of the main peak in TSL glow curves (Fig. 6). Moreover, the decay of EPR signals at room temperature (Fig. 8(b) and (e)) implies the involvement of these trapping states in the PersL of the investigated $Pr^{3+}$-doped complex phosphate materials.

### 3.5. Applications for anti-counterfeiting

Building on the earlier discussion of the dynamic multicolor and multimodal properties of $Pr^{3+}$-doped $Ba_3Lu(PO_4)_3$ and $Sr_3Lu(PO_4)_3$ materials, we propose designing a luminescent anti-counterfeiting label. Powder samples can be used to make ink for screen printing.[54,55] An example of a multicolor anti-counterfeiting image printed on a banknote is shown in Fig. 9. When excited at 444 nm, UC luminescence in the UV range is produced, which is invisible to the naked eye and requires specialized equipment to detect. Under X-ray exposure, the label appears pink, especially at low $Pr^{3+}$doping levels in $Ba_3Lu(PO_4)_3$. Once X-rays are stopped, the PersL signal is still observable, but its spectrum differs from that of XRL, shifting the color from pink to pure red. PersL can last for several hours, and if the intensity drops below detection, heating the item can release trapped charges, causing a brief spike in luminescence as the TSL signal emerges. Additionally, $Pr^{3+}$ ions can be excited with UV and visible light to produce classical PL with distinct spectral and decay profiles. This multimodal, time-resolved luminescence is very difficult to replicate with conventional phosphors, providing a high level of anti-counterfeiting security. Overall, these materials demonstrate remarkable versatility as anti-counterfeiting solutions.

## 4. Conclusions

This work establishes $Pr^{3+}$-doped eulytite-type phosphates as single-phase, multimodal luminescent platforms that uniquely combine blue-light-driven UVC UC with X-ray-triggered PersL within a single host lattice, enabling excitation-selective emission pathways governed by defect-mediated recombination and energy-transfer processes.

$Pr^{3+}$-doped $Ba_3Lu(PO_4)_3$ and $Sr_3Lu(PO_4)_3$ phosphors were shown to combine multiple luminescence mechanisms within a single material system, including blue-to-UVC UC, UV-VIS PL, XRL, red PersL, and TSL. Efficient UVC UC under 444 nm excitation originates from an excited-state absorption process in $Pr^{3+}$ ions, while X-ray excitation selectively populates lower-lying $Pr^{3+}$ states through defect-mediated recombination

pathways, resulting in intense VIS emission without UVC contribution.

TSL investigations reveal that charge trapping in both host lattices is governed by a quasi-continuous distribution of defect states rather than discrete trap levels. Trap depths determined by $T_{max}$–$T_{stop}$ and IRA fall within 0.9–1.15 eV, which is close to the optimal range for room-temperature PersL. EPR spectroscopy confirms the formation of radiation-induced phosphorus-related radical centers and additional shallow traps, likely $F^+$-type centers, whose thermal stability overlaps with the main TSL glow peak, demonstrating their direct involvement in the PersL process.

Overall, we conclude that $Ba_3Lu(PO_4)_3$ and $Sr_3Lu(PO_4)_3$ hosts exhibit comparable trap structures, resulting in similar PersL performance under identical conditions. The $Ba_3Lu(PO_4)_3$-based phosphor exhibits higher UC intensity and a more pronounced color contrast between XRL and persistent emission, enhancing its functional versatility. This host-dependent tuning of multimodal emission behavior highlights $Ba_3Lu(PO_4)_3$: $Pr^{3+}$ as a particularly promising candidate for next-generation anti-counterfeiting and information encryption applications.

## Conflicts of interest

There are no conflicts to declare.

## Data availability

The data supporting this study have been included within the article and the corresponding supplementary information (SI). Supplementary information provides Rietveld refinement patterns of XRD data of the samples. See DOI: https://doi.org/10.1039/d6tc00314a.

## Acknowledgements

This project received funding from the Research Council of Lithuania (LMTLT), agreement No. S-PD-24-62. AA and DS acknowledge the donation from SIA ''Mikrotīkls'' (MikroTik), administered by the University of Latvia Foundation, project No. 2326. AG appreciates the Polish Academy of Sciences for its support through the PAN-NANU (PAS-NASU) program for scientists collaborating with INTiBS PAN, NR thanks project no. UMO-2025/57/B/ST4/00594. During the preparation of this work, the authors used Grammarly typing assistant in order to improve language and readability. After using this tool, the authors reviewed and edited the content as needed and take full responsibility for the content of the publication. Declaration of generative AI and AI-assisted technologies in the writing process.

## References

1 X. Yu, H. Zhang and J. Yu, *Aggregate*, 2021, **2**, 20–34.
2 K. Pushpendra and B. S. Naidu, *Adv. Colloid Interface Sci.*, 2025, **341**, 103480.
3 C. Zhang, Q. Yin, S. Ge, J. Qi, Q. Han, W. Gao, Y. Wang, M. Zhang and J. Dong, *Mater. Res. Bull.*, 2024, **176**, 112801.
4 S. Tian, P. Feng, S. Ding, Y. Wang and Y. Wang, *J. Alloys Compd.*, 2022, **899**, 163325.
5 Y. Hu, S. Li, S. Yu, S. Chen, Y. Yan, Y. Liu, Y. Chen, C. Chen, Q. Shao and Y. Liu, *Nanomaterials*, 2022, **12**, 3123.
6 L. Liu, S. Peng, Y. Guo, Y. Lin, X. Sun, L. Song, J. Shi and Y. Zhang, *ACS Appl. Mater. Interfaces*, 2022, **14**, 41215–41224.
7 Y. Zhang, X. Shan, X. Lv, D. Chen, S. Miao, W. Wang and Y. Liang, *Chem. Eng. J.*, 2023, **474**, 145886.
8 R. Senthamarai, Z. Zhao, C. Liu, L. Wang and J. Zhang, *Coord. Chem. Rev.*, 2025, 542, 216892.
9 G. Doke, P. Rodionovs, A. Antuzevics, M. Kemere, G. Krieke, A. Zarkov, A. Beganskiene and M. Back, *Opt. Mater.*, 2026, **170**, 117727.
10 J. Jiang, R. Bai, C. Liu, J. Zhang and L. Wang, *J. Alloys Compd.*, 2023, **935**, 167963.
11 H. Ren, R. Bai, C. Liu, J. Zhang and L. Wang, *J. Lumin.*, 2023, **263**, 120057.
12 H. Ren, F. Huang, J. Jiang, L. Wang and J. Zhang, *Chem. Eng. J.*, 2022, **427**, 132023.
13 M. Leimane, V. Vitola, K. Laganovska, E. Einbergs, M. Dile and A. Zolotarjovs, *Materialia*, 2025, **41**, 102426.
14 K. Van Den Eeckhout, A. J. J. Bos, D. Poelman and P. F. Smet, *Phys. Rev. B: Condens. Matter Mater. Phys.*, 2013, **87**(4), 045126.
15 J. Zhang, R. Liu, X. Fu, J. Yi, T. Lin, Z. Liu, N. Chen and H. Zhang, *J. Am. Ceram. Soc.*, 2025, **108**(2), DOI: 10.1111/jace.20204.
16 Q. Du, J. Ueda and S. Tanabe, *J. Mater. Chem. C Mater.*, 2023, **11**, 16225–16233.
17 T. Förster, J. Reifenberger, T. Moumin, J. Helmbold, Ž. Antić, M. D. Dramićanin and M. Suta, *Chem. Sci.*, 2025, **16**, 12309–12323.
18 X. Ma, P. Feng, Y. Wang, S. Ding, S. Tian and Y. Wang, *J. Mater. Chem. C Mater.*, 2022, **10**, 1105–1117.
19 E. Pavitra, G. Seeta Rama Raju and J. S. Yu, *J. Alloys Compd.*, 2014, **592**, 157–163.
20 Z. Yang, Y. Sun, Q. Xu and J. Sun, *J. Rare Earths*, 2015, **33**, 1251–1255.
21 N. Rebrova, R. Lisiecki, P. Zdeb-Stańczykowska, Y. Zorenko, A. Voloshinovskii, A. Pushak and P. J. Dereń, *J. Phys. Chem. C*, 2025, **129**, 1873–1884.
22 Z. Yang, D. Xu, J. Sun, J. Du and X. Gao, *Mater. Sci. Eng., B*, 2016, **211**, 13–19.
23 M. Xie, W. Ruan and J. Wang, *J. Lumin.*, 2020, **224**, 117278.
24 N. Rebrova, A. Grippa, P. Zdeb-Stańczykowska and P. J. Dereń, *Inorg. Chem.*, 2025, **64**, 11146–11154.
25 M. P. Pechini, 3330697, 1967.
26 J. Barbier, *J. Solid State Chem.*, 1992, **101**, 249–256.
27 Z. Wang, Z. Xia, M. S. Molokeev, V. V. Atuchin and Q. Liu, *Dalton Trans.*, 2014, **43**, 16800–16804.
28 N. Rebrova and B. Bondzior, *Spectrochim. Acta, Part A*, 2025, **343**, 126523.
29 P. Zdeb, N. Rebrova and P. J. Dereń, *J. Phys. Chem. Lett.*, 2024, **15**, 9356–9360.
30 X. Wang and Y. Mao, *J. Mater. Chem. C*, 2022, **10**, 3626–3646.

 

31 B. Wang, H. Lin, J. Xu, H. Chen, Z. Lin, F. Huang and Y. Wang, *Inorg. Chem.*, 2015, **54**, 11299–11306.
32 F. Auzel, *Chem. Rev.*, 2004, **104**, 139–174.
33 P. Xiong, C. Zheng, M. Peng, Z. Zhou, F. Xu, K. Qin, Y. Hong and Z. Ma, *J. Am. Ceram. Soc.*, 2020, **103**, 6922–6931.
34 T. Wang, J. Gou, X. Xu, D. Zhou, J. Qiu and X. Yu, *Opt. Express*, 2015, **23**, 12595.
35 T. Zorenko, V. Gorbenko, S. Nizankovskiy and Y. Zorenko, *Acta Phys. Pol. A*, 2018, **133**, 948–953.
36 W. Drozdowski and A. J. Wojtowicz, *J. Alloys Compd.*, 2000, **300–301**, 261–266.
37 P. Zdeb-Stańczykowska, N. Rebrova, Y. Zorenko, A. Voloshinovskii, A. Pushak and P. J. Dereń, *J. Alloys Compd.*, 2025, **1016**, 178807.
38 M. A. Gusowski, H. C. Swart, L. S. Karlsson and M. Trzebiatowska-Gusowska, *Nanoscale*, 2012, **4**, 541–546.
39 E. Gardenali Yukihara, *Ceram. Int.*, 2023, **49**, 24356–24369.
40 E. G. Yukihara, A. C. Coleman, R. H. Biswas, R. Lambert, F. Herman and G. E. King, *Radiat. Meas.*, 2018, **120**, 274–280.
41 A. Bos, *Materials*, 2017, **10**, 1357.
42 A. J. J. Bos, *Radiat. Meas.*, 2006, **41**, S45–S56.
43 G. Doke, G. Krieke, P. Rodionovs, D. Nilova and A. Antuzevics, *J. Rare Earths*, 2025, **43**, 676–683.
44 F. Sun, R. Xie, L. Guan and C. Zhang, *J. Lumin.*, 2016, **180**, 251–257.
45 S. W. S. McKeever, *Thermoluminescence of Solids*, Cambridge University Press, 1985.
46 V. Natarajan, M. K. Bhide, A. R. Dhobale, S. V. Godbole, T. K. Seshagiri, A. G. Page and C.-H. Lu, *Mater. Res. Bull.*, 2004, **39**, 2065–2075.
47 N. Y. Garces, K. T. Stevens, L. E. Halliburton, S. G. Demos, H. B. Radousky and N. P. Zaitseva, *J. Appl. Phys.*, 2001, **89**, 47–52.
48 A. Antuzevics, G. Doke, G. Krieke, J. Stadulis, A. Beganskiene, A. Kareiva, C.-Y. Su, H.-W. Fang and A. Zarkov, *J. Alloys Compd.*, 2025, **1012**, 178525.
49 P. Fattibene and F. Callens, *Appl. Radiat. Isot.*, 2010, **68**, 2033–2116.
50 A. S. Marfunin, *Spectroscopy, Luminescence and Radiation Centers in Minerals*, Springer Berlin Heidelberg, Berlin, Heidelberg, 1979.
51 G. Krieke, A. Antuzevics, A. Kalinko, A. Kuzmin, T. Murauskas, A. Kareiva and A. Zarkov, *J. Mater. Chem. C*, 2024, **12**, 16989–16998.
52 B. Henderson, *Crit. Rev. Solid State Mater. Sci.*, 1980, **9**, 1–60.
53 Z. Zou, J. Weng, C. Liu, Y. Lin, J. Zhu, Y. Sun, J. Huang, G. Gong and H. Wen, *Crystals*, 2024, **14**, 431.
54 S. Yu, X. Gong, D. Shi, M. Xue, Y. Zhang, K. Han, N. Li, G. Hou and F. Li, *Opt. Mater.*, 2024, **157**, 116157.
55 B.-M. Liu, Y. Lin, Y. Liu, B. Lou, C.-G. Ma, H. Zhang and J. Wang, *Light: Sci. Appl.*, 2024, **13**, 286.